Characteristics of a pulsed hollow cathode discharge operated in an Ar+O$_2$ gas mixture and deposition of copper nickel oxide thin films

Anna Kapran [a,b], Rainer Hippler [a,c,*], Harm Wulff [c], Jiri Olejnicek [a], Aneta Pisarikova [a,d], Martin Cada [a], Zdenek Hubicka [a]

[a] *Institute of Physics, Czech Academy of Sciences, Na Slovance 2, 18200 Prague, Czech Republic*
[b] *Charles University, Faculty of Mathematics and Physics, Ke Karlovu 3, 12116 Prague, Czech Republic*
[c] *Institut für Physik, Universität Greifswald, Felix-Hausdorff-Str. 6, 17489 Greifswald, Germany*
[d] *Joint Laboratory of Optics, Palacky University Olomouc, Av. 17. listopadu 50A, 77207 Olomouc, Czech Republic*

ARTICLE INFO

ABSTRACT

A hollow cathode discharge with a CuNi (Cu50Ni50) cathode is operated inside a vacuum chamber with Ar gas flowing through its nozzle. O$_2$ gas is admitted to the vacuum chamber. Typical Ar+O$_2$ gas pressures are in the range of 2–50 Pa. The energy distribution of plasma ions is investigated with the help of energy-resolved mass spectrometry. Singly charged Ar$^+$ and molecular O$_2^+$ ions are the most abundant ionic species. Deposition rate and heat flux to a substrate increase as function of discharge current. At high pressures, the deposition rate is further increased by the directional gas flow, which becomes more focused onto the substrate. Deposited and annealed thin films are analysed by X-ray diffraction and Raman spectroscopy. As-deposited films are composed of a mixed Cu$_x$Ni$_{1-x}$O cubic phase with a preferred (111) orientation. Upon annealing at 600 °C, the mixed Cu$_x$Ni$_{1-x}$O phase separates into two sub-phases composed of NiO and CuO. Annealed films display a photoelectrochemical (PEC) activity as a photocathode. The PEC activity deteriorates with time, however. This behaviour is related to the reduction of CuO to Cu$_2$O.

1. Introduction

Mixed metal oxides (MMO) are novel compounds composed of two or more metallic elements combined with oxygen to form an oxide. Examples include copper and nickel ferrites (CuFe$_2$O$_4$ and NiFe$_2$O$_4$), nickel and zinc cobaltites (CoNiO$_2$ and CoZnO$_2$), and magnesium aluminate (MgAl$_2$O$_4$). In general, these compounds offer unique properties that result from a combination of the different metallic elements and can be used in a variety of applications, such as catalysts [1–5], ceramics [6–10], sensors [11–14], and batteries [15–18].

Mixed copper nickel oxides have attracted some interest in recent years. CuO and NiO are p-type semiconductors, in contrast to most other metal oxides which are of n-type [14,19]. The band gaps of CuO (1.7 eV) and NiO (3.5 eV) are very different [19] while the work functions of CuO (6.0 eV) and NiO (6.4 eV) are close to each other [20]. Both materials fulfil the requirements as a photocatalyst, i.e., a theoretical minimum band gap energy of 1.23 eV for water splitting applications and with respect to the energetic positions of valence band and conduction band [21,22]. Cu$_x$Ni$_{1-x}$O MMOs with $x = 0-1$ have band gaps that lie between those of CuO and NiO and thus allow the band gap to be tailored by varying the Cu/Ni ratio [23–26].

The electrical conductivity also depends on the Cu/Ni ratio; it increases with increasing copper content x [23,24,27]. Copper nickel oxides have many applications, e.g., as glucose sensors [28], for photocatalytic degradation of volatile organic compounds [29], in solar cells [30], and as catalyst for oxidation of CO [31], degradation of phenol [32], NO$_x$ removal [33], and water splitting [34].

In the present communication we investigate a pulsed hollow cathode (PHC) discharge with a copper nickel cathode. A typical hollow cathode (HC) is made from a cylindrical tube. The discharge is sustained by electrons which undergo a pendulum motion inside the HC [35–38]. Beside thin film deposition, the HC discharge has been employed in, e.g., atomic spectroscopy, laser technology, and as UV generator [37,39–46]. Here we focus on two major goals: an investigation of the PHC discharge with respect to its suitability for deposition of MMO films and the deposition and characterization of mixed copper nickel oxide films. Characterization of the PHC discharge is carried out with the help of time- and energy-resolved mass spectrometry, time-resolved optical emission spectroscopy, and with a multi-functional plasma sensor to measure heat flux and deposition rate. The discharge is then utilized for deposition of copper nickel oxide thin
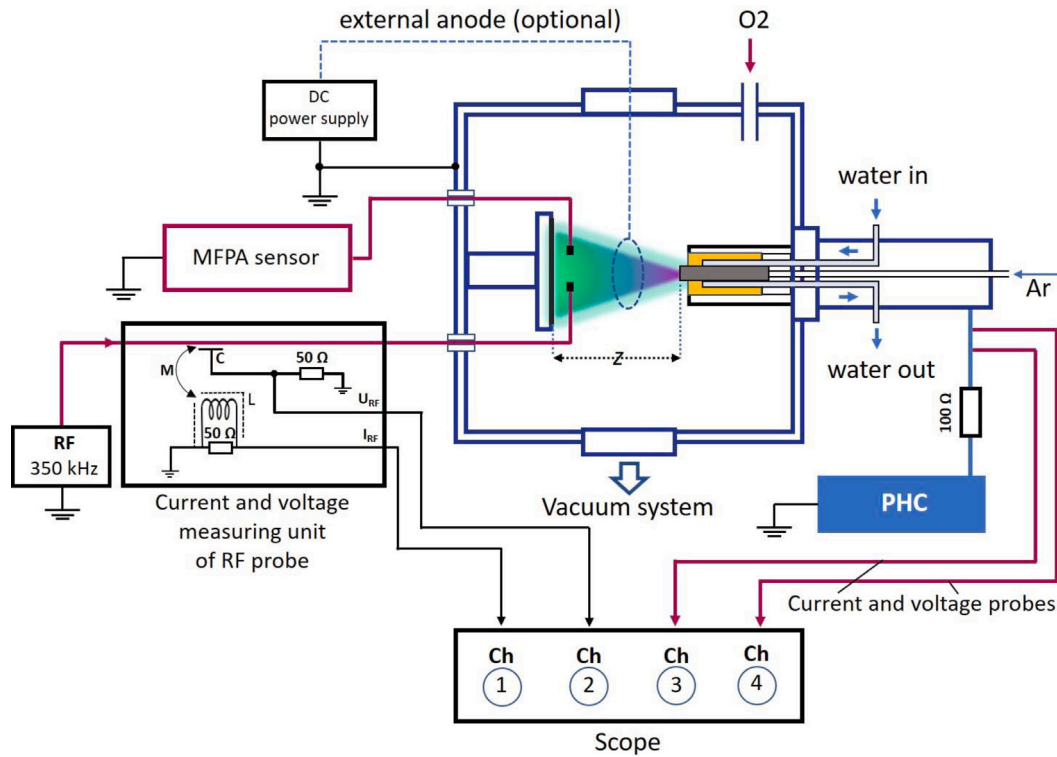
Fig. 1. Experimental set-up (schematic) for thin film deposition with hollow cathode, power supply (PHC) with 100 Ω resistor, external anode (optional), substrate holder, MFPA sensor, and RF probe (optional) inside the vacuum chamber.

films on silicon Si(111) wafers and on fluorine-doped tin oxide (FTO) coated glass substrates. The structural and morphological properties of the as-deposited and annealed films are studied with the help of X-ray diffractometry and Raman spectroscopy. The photoelectrochemical (PEC) activity is further investigated.

2. Experiment

The experimental set-up consists of a cylindrical hollow cathode inside a vacuum chamber of 35 cm in diameter and 19 cm of height. The chamber is pumped by a combination of a rotary and a turbomolecular pump to a base pressure of 1×10^{-4} Pa. The nozzle is made from copper nickel (Cu50Ni50) alloy with a purity of 99.95%, a length of 40 mm, an outer diameter of 12 mm, and an inner diameter of 5 mm. The nozzle is embedded in a water-cooled copper holder. It protrudes out of the cooling holder, thus causing the end of the nozzle to heat up during operation [47–50]. The scheme of the HC sputtering system is depicted in Fig. 1.

The hollow cathode is connected via a 100 Ω resistor to a DC power supply (Advanced Energy MDX-500) and a home-made pulse power supply with a capacitor bank. This resistor acts as a discharge stabilizer to prevent unwanted discharge oscillations or arc ignition. The power switch allows to operate the HC discharge in pulsed mode. A commercial arbitrary waveform generator (OWON AG 1022) is employed to set the repetition frequency to $f = 5$ kHz and the pulse length to $T_{on} = 100$ µs. The pulsed hollow cathode (PHC) discharge is operated in current control mode with a typical mean discharge current of 0.25 A and a typical mean discharge power of about 80 W. The discharge characteristics are presented in a Fig. 2.

An additional ring anode made from a DN 63 CF copper gasket (inner diameter 63 mm, outer diameter 82 mm, thickness 2 mm) is mounted at a distance of 100 mm from the cathode [50]. The anode is powered by a regulated laboratory DC voltage supply (Manson HCS-3204) with a maximal output voltage of 60 V. The anode is kept at

ground potential (+0 V) during film deposition and at +60 V during the ion energy distribution measurements which are described below.

The gas flow rate of the working gases are adjusted using separate mass flow controllers. Argon (purity 99.996%) is introduced into the chamber through the hollow cathode at a flow rate of 200 sccm. The oxygen inlet is placed separately from the cathode nozzle, at the lateral side of the chamber in order to prevent poisoning of the cathode. In this way, the discharge is operated in metallic rather than in compound (oxidized) mode. The oxygen gas flow rate is set as 100 sccm (O_2 purity 99.999%).

The gas pressure *inside* the nozzle is determined by the gas flow rate Q through the tube

$$Q = L\Delta p = L(p_1 - p_2) \tag{1}$$

where p_1 and p_2 is the gas pressure at the tube's inlet and outlet, respectively, $\Delta p = p_1 - p_2$, and L the conductance. In the laminar regime, which can be used as a good approximation, the conductance of a straight tube with inner diameter d and length l is given by [51,52]

$$L = \frac{\pi d^4}{128\,\eta\,l}\,\bar{p} = \frac{\pi d^4}{256\,\eta\,l}\,(p_1 + p_2) \tag{2}$$

where $\bar{p} = \frac{1}{2}(p_1 + p_2)$ is the mean pressure, and η is the temperature-dependent gas viscosity [53]. Combining Eqs. (1) and (2) we obtain

$$Q = \frac{\pi d^4}{256\,\eta\,l}\,(p_1^2 - p_2^2). \tag{3}$$

With the help of Eq. (3), the mean gas pressure $\bar{p}$ for a given gas flow rate Q as function of chamber pressure p_2 is calculated. For a given gas flow rate Q, Fig. 3 shows the calculated mean gas pressure $\bar{p}$ as function of outlet pressure p_2 which is set equal to the chamber pressure for different gas (nozzle) temperatures. The gas pressure inside the nozzle increases when the chamber pressure is raised as was done during the experiments. For a typical nozzle temperature of 700 K and a chamber
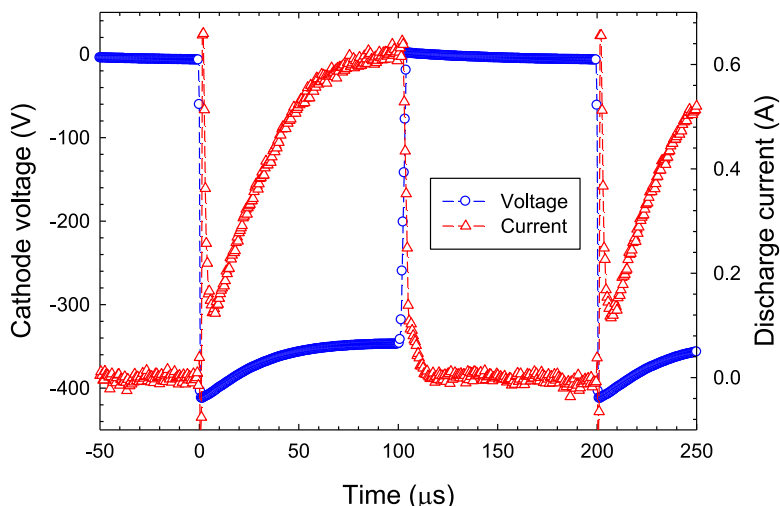
Fig. 2. Discharge voltage and discharge current *versus* time. The PHC discharge is operated with a Co50Ni50 nozzle, a pulse length of 100 μs, and a repetition frequency of 5 kHz. Mean discharge current 0.25 A. Argon gas flow rate 200 sccm, oxygen gas flow rate 100 sccm, gas pressure $p = 2.8$ Pa.
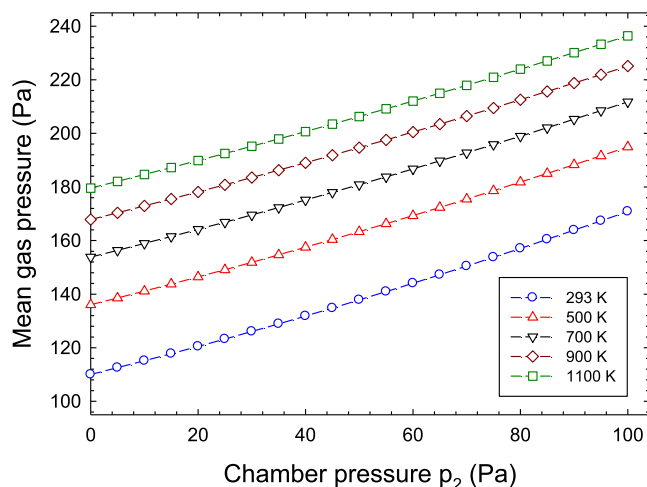

Fig. 3. Mean gas pressure $\bar{p}$ inside the HC nozzle as function of nozzle outlet (chamber) pressure p_2 and for different nozzle temperatures. Argon gas flow rate 200 sccm.

Table 1
Calculated transit time τ through the mass/energy analyzer.

Ion m/z	O$^+$ 16	Ar$^+$ 40	Ni$^+$ 58	Cu$^+$ 65
τ (μs)	47.5	75.1	90.4	95.8

Table 2
Relative abundance of nickel and copper isotopes [57].

Isotope mass	Ni					Cu	
	58	60	61	62	64	63	65
Abundance (%)	68.1	26.2	1.1	3.6	0.9	69.2	30.8

angle of 45 degree with respect to the target surface. Time-resolved OES measurements are performed with a gate width of 10 μs and with incremental gate steps of 10 μs.

The heat flux onto the substrate is measured with the help of a multi-functional probe analyzer (MFPA) diagnostics system (OUT, Berlin) featuring a quartz microbalance for deposition rate and a thermopile for heat flux measurements [58]. The probe is placed in front of the nozzle at the substrate position.

The deposition is done on Si (111) or FTO substrates. Si(111) substrates (about 15 mm × 20 mm) are diced from a p-type silicon wafer with a (111) crystallographic orientation. Likewise, soda lime glass substrates coated with conductive fluorine doped tin oxide (FTO) layer (7 $\Omega/\square$, TCO22-7/LI, Solaronix) are employed. Prior to deposition, all substrates were cleaned by bath sonification in acetone, treated in ethanol and then rinsed in distilled water for 10 min respectively. All deposition experiments are carried out at two different gas pressures of 2.8 Pa and 50 Pa in the vacuum chamber. The gas pressure is measured with a capacitance vacuum gauge. The required pressure in the chamber is adjusted and maintained constant by the valve between chamber and turbomolecular pump. Films on Si(111) and FTO substrates are deposited for 60 mins and 90 mins, respectively. Based on measurements with the MFPA sensor, the typical deposition rate (film thickness) at 2.8 Pa and 50 Pa is 1.8 nm/min (120 nm) and 5 nm/min (300 nm), respectively, for a deposition time of 60 min.

The as-deposited samples are exposed to an annealing procedure using an annealing oven regulated by Classic Clare 4.0 controller. The annealing procedure was done at temperatures of 410 °C and 600 °C. The annealing protocol uses the following parameters: heating rate of 5 °C per minute and maximum temperature is held for 240 min.

To determine and characterize the crystallography of studied samples, the X-ray diffraction (XRD) technique is employed. This analysis is done with the PANalytical Empyrean X-ray diffractometer operating in Grazing Incidence (GI) geometry with Cu Kα radiation ($\lambda = 0.154$ nm) in a typical 2θ range from 10° to 100° and with a step size of 0.02°. Raman spectroscopy is carried out at room temperature using a Renishaw Raman Microscope RM 1000 with a polarized beam of an Ar$^+$ ion laser ($\lambda = 514.5$ nm) in the back-scattering configuration.
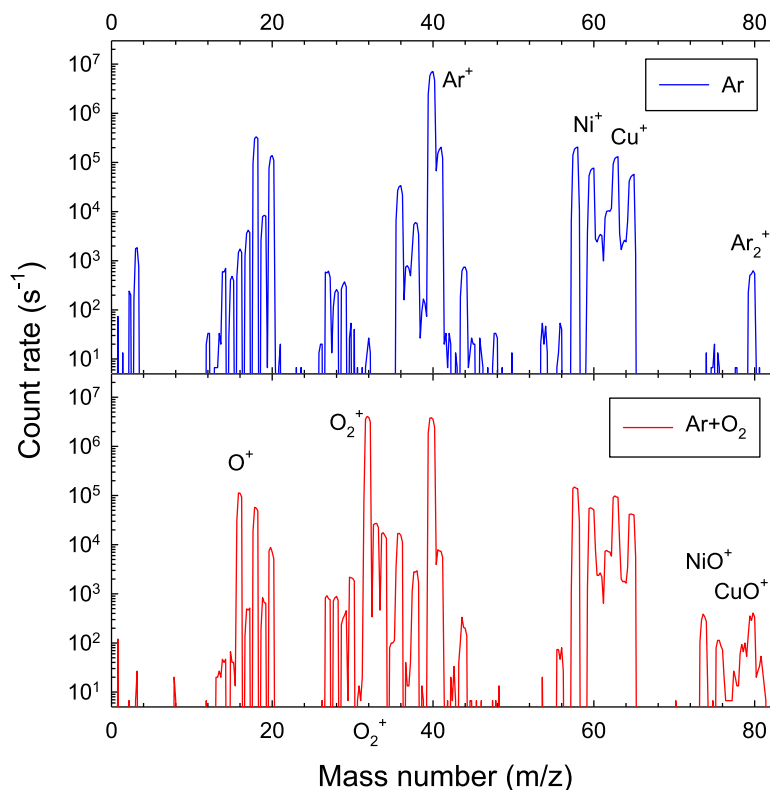
pressure of 50 Pa, the mean pressure inside the tube is about 175 Pa which agrees reasonable with an estimate of Hubicka et al. [54].

Energy-resolved mass spectrometry is performed with a commercial Hiden EQP 1000 mass/energy analyzer (Hiden Analytical Ltd., UK) [55, 56]. The instrument is mounted opposite to the hollow cathode and the anode at a distance of 120 mm from the anode (Fig. 1). The transit time of ions through the mass analyser is calculated with the help of a spread-sheet provided by the manufacturer. Calculated transit times for different ions are given in Table 1.

Optical emission spectroscopy (OES) is carried out with a Shamrock SR500D spectrometer (focal length 500 mm) equipped with an iCCD detector (iStar DH334T18UE3, Andor Technology, Belfast, Northern Ireland). The spectrometer is equipped with three gratings and with a filter wheel in front of the entrance slit to suppress second order lines. An optical fibre connected to the entrance slit (slit width 10 μm) of the spectrometer is installed outside the vacuum chamber at an

Fig. 4. Mass spectrum from Ar and Ar+O$_2$ gas mixture. Ar gas flow rate 200 sccm, O$_2$ gas flow rate 10 sccm, gas pressure 2.1 Pa, discharge current 0.25 A.

The optical transmission of deposited films is measured with a spectrophotometer (LAMBDA 1050 UV/Vis/NIR, Perkin-Elmer). The photoelectrochemical (PEC) activity is measured in an electrochemical cell equipped with quartz glass. The electrodes are connected to a potentiostat (OGF 500, Origaflex) in three-electrode configuration. The working electrode consists of the Ni-Cu-O layer on FTO-coated glass, the counter electrode is a platinum plate (1 cm × 1 cm), and the reference electrode is Ag/AgCl (sat. KCl, +197 mV vs. SHE). The electrochemical characteristics are measured in an aqueous electrolyte of 0.1 mol/l Na$_2$SO$_4$ (Penta chemicals). Linear voltammetry is measured under chopped (5 s *on*, 5 s *off*) simulated solar light using a Xe lamp with AM 1.5 filter (Hamamatsu C4251) with an intensity of 62 mW/cm^2. Amperometry is measured for 2 min in the dark while during the remaining time the samples are illuminated with the same light source as in the linear voltammetry measurements.

3. Results and discussion

3.1. Mass spectrometry

Typical ion mass spectra for a PHC discharge operated in pure Ar and in an Ar+O$_2$ gas mixture are displayed in Fig. 4. The kinetic energy of detected ions is set to 1 eV. The mass spectrum from pure Ar is dominated by singly-charged Ar$^+$ ($m/z = 40$), Ni$^+$ ($m/z = 58$ and 60) and Cu$^+$ ($m/z = 63$ and 65) ions (see Table 2). The mass spectrum from the Ar+O$_2$ gas mixture additionally displays O$^+$, O$_2^+$, NiO$^+$, and CuO$^+$ ions. The intensity of Ni$^+$ and Cu$^+$ ions reduces by about 30 % when O$_2$ is added to the discharge which is not compensated by the appearance of CuO$^+$ and NiO$^+$ ions.

Fig. 5 compares ion energy distributions of singly charged O$^+$ ($m/z = 16$), O$_2^+$ ($m/z = 34$) Ar$^+$ ($m/z = 36$), Ni$^+$ ($m/z = 58$), and Cu$^+$ ($m/z = 63$). A positively biased anode to enhance the ion signal is employed. The intensity maximum (peak) of the distributions occurs at a kinetic energy close to $E = e_0 V_a$, where e_0 is the elementary

charge and $V_a = 60$ V is the applied anode voltage. Ar$^+$ ions display a pronounced low-energy tail which is caused by charge changing reactions [59].

In addition to the main peak at ≈60 eV, the energy distribution of O$^+$ ions displays a pronounced low-energy maximum which peaks at ≈45 eV. Also noticed is a pronounced high-energy tail above 60 eV observed for O$^+$ ions which could originate from dissociate ionization of O$_2$ molecules. The observed structures could originate from in-flight dissociation of a molecular ion via the formation of an intermediate repulsive O$_2^{+*}$ ion state, i.e., O$_2^{+*} \rightarrow$ O$^+$ + O [61].

Time-resolved measurements show a variation of the ion signal as function of time which follows the time evolution of the pulsed discharge (Fig. 6). The calculated transit time though the mass/energy filter (Table 1) was subtracted. Evidently, some *smearing-out* occurs which is attributed to the relatively broad energy distribution of the ions. The intensity variation is more pronounced for O$^+$ and Ar$^+$ ions compared to Cu$^+$ and Ni$^+$ ions.

3.2. Optical emission spectroscopy

Optical emission spectra are displayed in Fig. 7. Two emission spectra in the wavelength regions 318–354 nm and 746–782 nm are shown. The *ultraviolet* region contains the main Cu I emission lines at 324.6 nm and 327.3 nm and several Ni I emission lines in the range 335–354 nm [62]. Particularly strong are the Ni I lines at 341.3 nm, 345.9 nm, 351.4 nm, and 352.3 nm. The *red* region contains several strong Ar I emission lines at 750.4 nm, 751.5 nm, 763.5 nm, and 772.4 nm and the O I triplet lines at 777.2/777.4/777.5 nm. The temporal evolution of these lines is shown in Fig. 8. The intensity of all investigated lines rises strongly during the *on* part of the pulsed discharge and drops off quickly in the *off* part. There is some indication of an afterglow as the intensity of, in particular, the Ar I line shows a gradual decrease. The contribution of the Cu I and Ni I metal lines to the afterglow is significantly weaker or even absent. This means that the afterglow should have a negligible impact on film deposition.
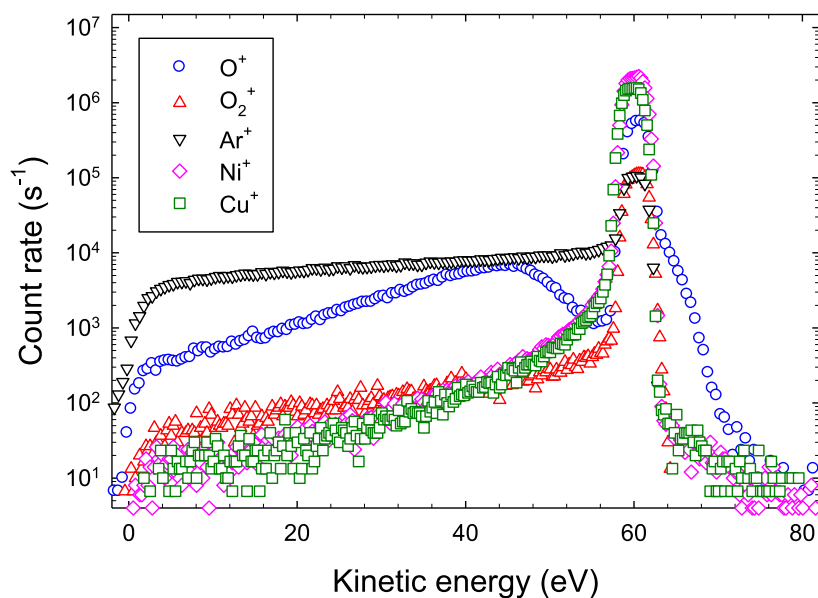
Fig. 5. Ion energy distribution of O$^+$ ($m/z = 16$, ○), O$_2^+$ ($m/z = 34$, △), Ar$^+$ ($m/z = 36$, ▽), Ni$^+$ ($m/z = 58$, ◇), and Cu$^+$ ($m/z = 63$, □) ions for a PHC discharge with a positively biased anode (+60 V) in an Ar+O$_2$ gas mixture. Ar gas flow rate 200 sccm, O$_2$ gas flow rate 10 sccm, gas pressure 2.1 Pa, discharge current 0.25 A.
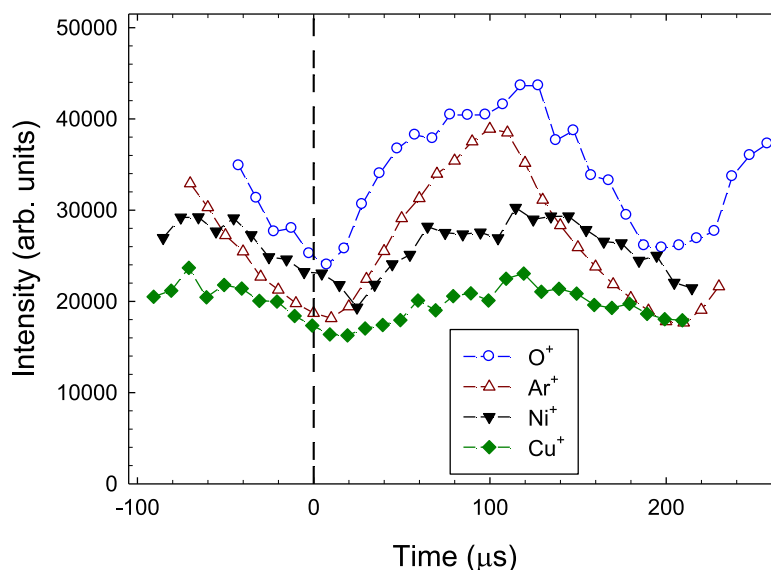

Fig. 6. Time-resolved energy-integrated intensity of O$^+$ (○), Ar$^+$ (△), Ni$^+$ (▽), and Cu$^+$ (◇) ions of an Ar+O$_2$ gas mixture of a pulsed hollow cathode discharge with a biased anode (+60 V). Ar gas flow rate 200 sccm, O$_2$ gas flow rate 10 sccm, gas pressure 2.1 Pa, discharge current 0.25 A.

Quantitatively, the behaviour of the optical lines follows that of the discharge current.

3.3. Deposition rate and heat flux

Deposition rate and heat flux measured with the multi-functional probe analyzer (MFPA) are displayed in Fig. 9 as function of discharge current. For the deposition rate a film density of 6.5 g cm^{-3} which is the average density of CuO and NiO was assumed. The deposition rate increases approximately linearly with discharge current whereas the heat flux is closer to a quadratic increase. Part of the heat flux increase is caused by impinging ions which show a similar tendency. The deposition rate increases with increasing pressure inside the vaccum chamber (Fig. 10). The increasing chamber pressure gives rise to an increasing gas density inside the nozzle of the plasma jet (Fig. 3) which results in a more focused gas flow towards the substrate, in agreement with observations of Sicha et al. [52,63,64].

4. Film characterization

4.1. Crystal structure and morphology

The crystalline structure of deposited thin films is investigated by grazing incidence X-ray diffraction (XRD). Fig. 11 shows XRD results for as-deposited and annealed (at 410 °C and 600 °C) films on Si(111) substrates deposited at gas pressures of 2.8 Pa and 50 Pa. We note in passing that the measured reflections of the film deposited at 50 Pa are larger compared to 2.8 Pa film which is due to the higher deposition rate (Fig. 10). As-deposited films are composed of a cubic lattice of Cu$_x$Ni$_y$O with a preferred (111) orientation and with a lattice parameter of 0.422 nm which is significantly larger compared to the reported lattice parameter for NiO of 0.4178 nm [65]. The annealed film (410 °C) deposited at the lower pressure (2.8 Pa) shows little difference to the as-deposited film while the annealed film deposited
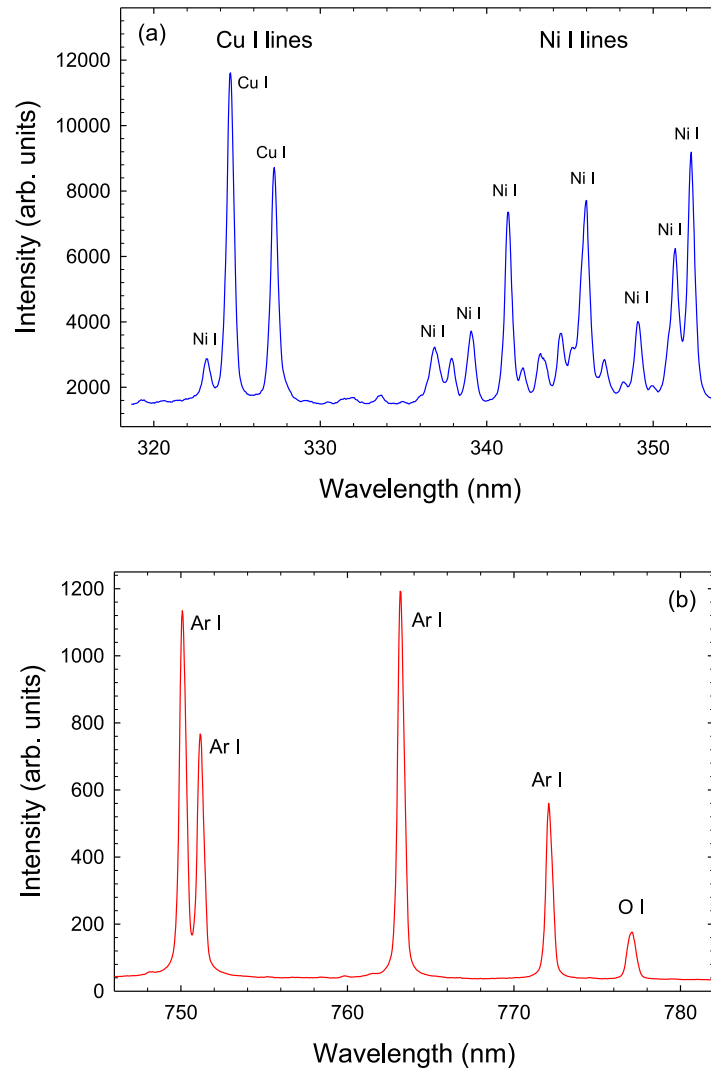
Fig. 7. OES spectrum from (a) 318–354 nm showing Cu I and Ni I emission lines and from (b) 746–782 nm showing Ar I and O I emission lines. Ar gas flow rate 200 sccm, O$_2$ gas flow rate 100 sccm, discharge current 0.25 A.
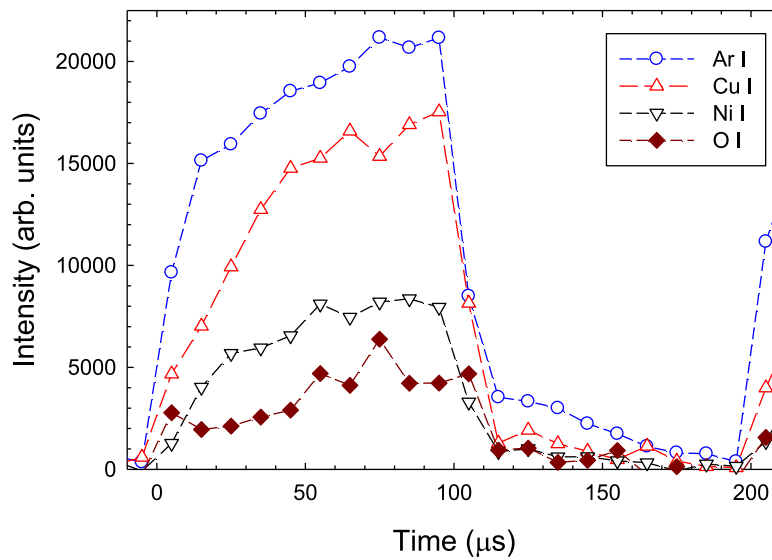

Fig. 8. Temporal evolution of Ar I 763 nm, Cu I 325/327 nm, Ni I 351/352 nm, and O I 777.2/777.4/777.5 nm emission lines. Ar gas flow rate 200 sccm. O$_2$ gas flow rate 100 sccm. Gas pressure 50 Pa. Discharge current 0.25 A.
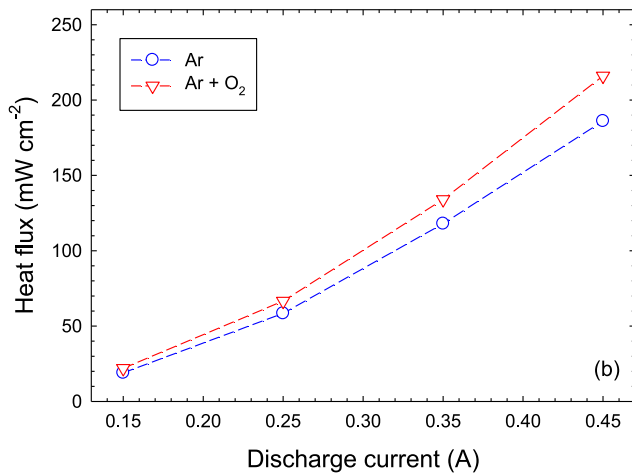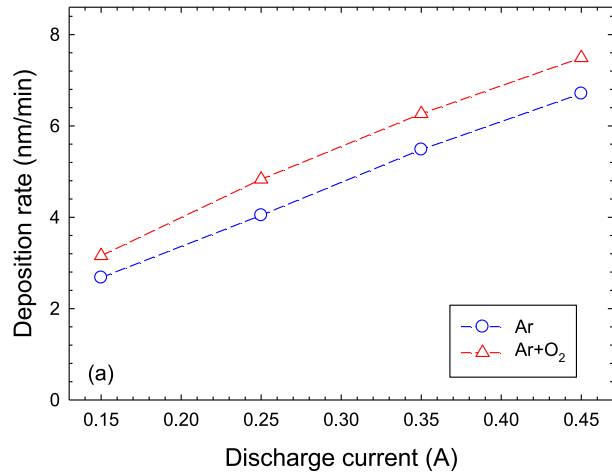
Fig. 9. (a) Deposition rate and (b) heat flux *versus* discharge current for a PHC discharge. Distance from HC 10.5 cm. Argon gas flow rate 200 sccm, argon gas pressure 2.1 Pa. Oxygen gas flow rate 100 sccm, Ar+O$_2$ gas pressure 2.8 Pa.
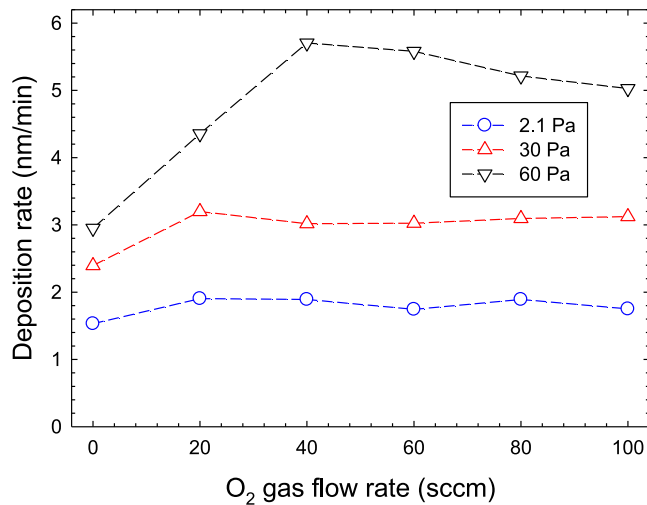

Fig. 11. GIXRD of as-deposited and annealed CuNiO films on Si(111) substrates deposited at (a) 2.8 Pa and (b) 50 Pa. Reflections from CuO (▲), NiO (▼), and Laue peaks (L) are indicated. Discharge current 0.25 A. Ar gas flow rate 200 sccm, O$_2$ gas flow rate 100 sccm.

Fig. 10. Deposition rate *versus* O$_2$ gas flow rate for a PHC discharge at different partial argon gas pressures of 2.1 Pa (○), 30 Pa (△), and 60 Pa (▽). Distance from HC 15 cm. Argon gas flow rate 200 sccm. Discharge current 0.35 A.
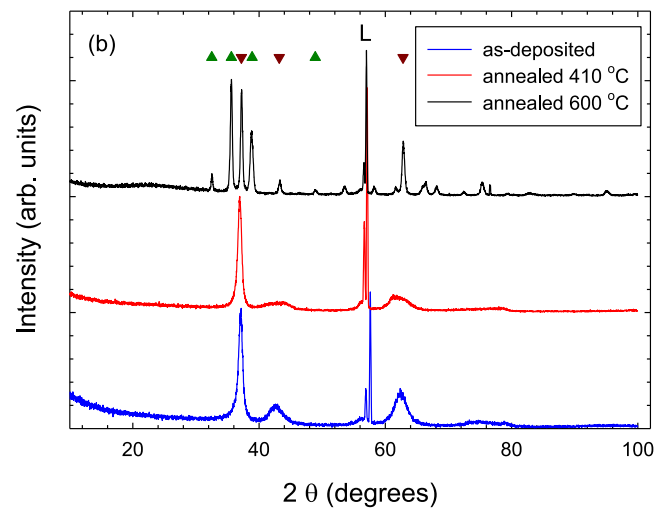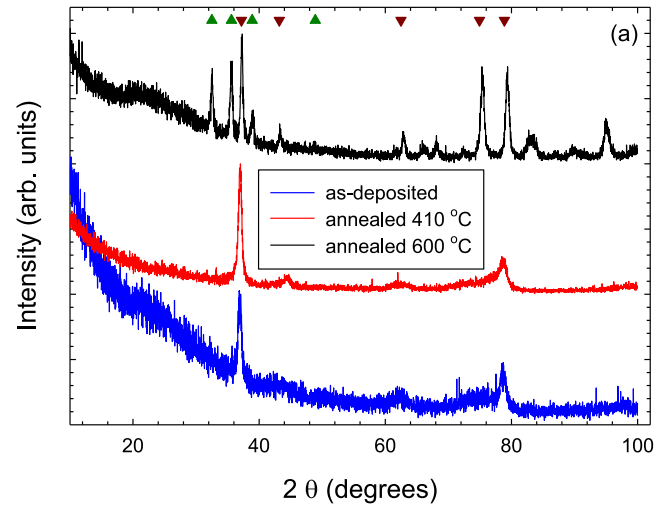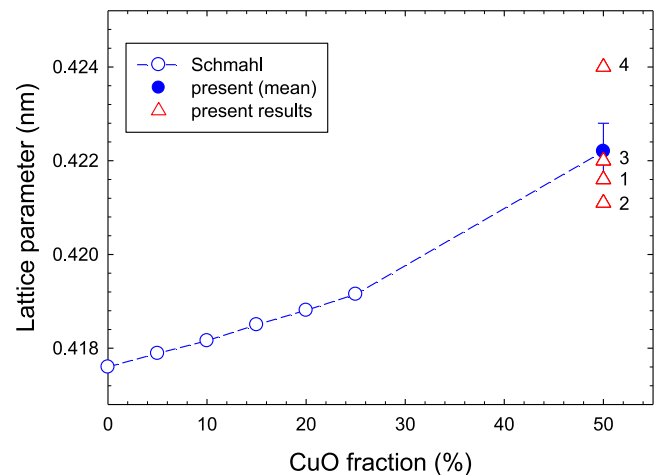

Fig. 12. Lattice parameter *a* of the mixed c-Cu$_x$Ni$_{1-x}$O phase as function of the CuO mol fraction *x*. Present results (△) for films A-as (1), A-410 (2), B-as (3), and B-410 (4) and of the mean value (●) are compared with results of Schmahl et al. (○) [60].
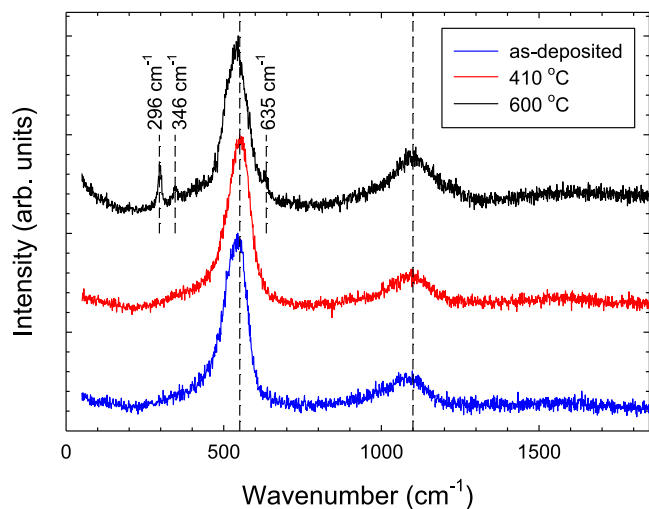
Fig. 13. Raman spectroscopy of as-deposited and annealed (410 °C, 600 °C) films deposited on FTO glass. Ar gas flow rate 200 sccm, O₂ gas flow rate 100 sccm, gas pressure 2.8 Pa. Discharge current 0.25 A. Deposition time 90 min.

Table 3
Crystalline phase and lattice parameters a, b, c, and β of as-deposited and annealed (410 °C, 600 °C) films deposited at 2.8 Pa (A-as, A-410, and A-600) and 50 Pa (B-as, B-410, and B-600). D mean particle size. cub: cubic, m: monocline.

Film	Crystalline phase	Lattice parameter (nm, degrees)		D
		present results	Reference	(nm)
A-as	cub-$Cu_xNi_{1-x}O$	$a = 0.4216$		13
A-410	cub-$Cu_xNi_{1-x}O$	$a = 0.422$		17
A-600	cub-NiO	$a = 0.4182$	$a = 0.41760$ [60]	107
	m-CuO	$a = 0.4695; b = 0.3409$	$a = 0.46837, b = 0.34226$	148
		$c = 0.5115; \beta = 99.44°$	$c = 0.51288, \beta = 99.54°$ [69]	
A-600-P	cub-NiO	$a = 0.4189$		50
	cub-Cu_2O	$a = 0.4253$	$a = 0.4267$ [70]	20
B-as	cub-$Cu_xNi_{1-x}O$	$a = 0.4212$		16
B-410	cub-NiO	$a = 0.418$		6
	cub-$Cu_xNi_{1-x}O$	$a = 0.422$		6
B-600	cub-NiO	$a = 0.4180$		80
	m-CuO	$a = 0.4703; b = 0.3417$		90
		$c = 0.5114; \beta = 99.3°$		
B-600-P	cub-NiO	$a = 0.4184$		101
	cub-Cu_2O	$a = 0.4269$		73

at the larger pressure (50 Pa) seem to show the beginning separation of the mixed Cu_xNi_yO phase into NiO and Cu_xNi_yO lattice phases with somewhat different lattice parameters of 0.418 nm and 0.424 nm. Films annealed at 600° show a different picture as can be seen by the appearance of several new diffraction peaks. These are related to a separation of the mixed Cu_xNi_yO phase into two sub-phases composed of NiO and CuO. For example, the reflections at 37.2°, 43.2°, and 62.8° are attributed to cubic NiO(111), NiO(200), and NiO(220) planes, respectively, whereas the reflections at 32.5°, 35.6°, 38.9°, and 48.9° belong to monoclinic CuO(110), CuO($\bar{1}$11), CuO(111), and CuO($\bar{2}$02) planes, respectively, [66,67]. A more detailed analysis reveals that the ratio of the two phases is not exactly one-to-one but has a small preference for CuO. A separation of the mixed oxide phase into two clearly separated CuO and NiO phases was also observed by Chen et al. [68].

The derived lattice parameters are provided in Table 3. Fig. 12 compares the lattice parameters of the present mixed cubic-$Cu_xNi_{1-x}O$ phase with previous results of Schmahl et al. [60]. The lattice parameter increases from $a = 0.4176$ nm for pure NiO to $a = 0.41915$ nm for $Cu_{0.25}Ni_{0.75}$ [60] and to $a \approx 0.4222$ nm for the present $Cu_{0.5}Ni_{0.5}O$ lattice.

The XRD results are supported by Raman spectroscopy. As-deposited and annealed Raman spectra are composed of two broad peaks at about
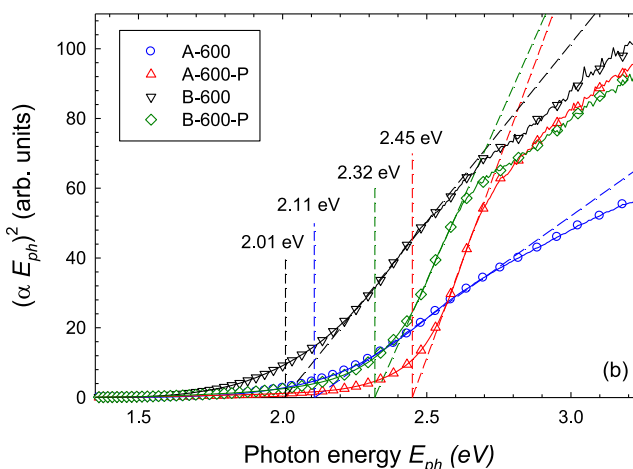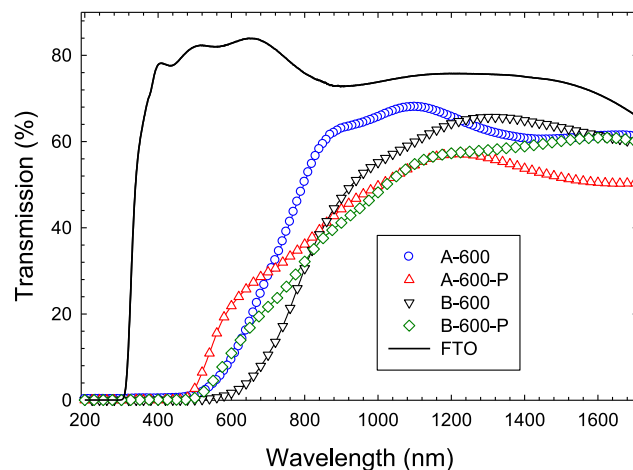

Fig. 14. (a) Transmission and (b) Tauc plot of annealed films (600 °C) deposited on FTO-coated glass at 2.8 Pa (A-600 ∘, A-600-P △) and 50 Pa (B-600 ▽, B-600-P ◇) prior to and after PEC (P) activity measurements.

550 cm⁻¹ and a weak feature at 1100 cm⁻¹ (Fig. 13). The peaks are frequently assigned to one-phonon LO and two-phonon TO vibrational modes associated with NiO [71,72]. However, in particular, the one-phonon LO mode at 550 cm⁻¹ mode is strongly suppressed in bulk NiO while it is enhanced in nano-crystalline NiO [73,74]. In addition, the presence of Cu/CuO could play a significant role here. The Raman spectra of the film annealed at 600° additional displays three sharp peaks at 296 cm⁻¹, 346 cm⁻¹, and 635 cm⁻¹ which are attributed to CuO [26,75,76].

4.2. Optical properties

The measured optical transmittance of annealed films A-600 and B-600 on FTO glass is displayed in Fig. 14(a). Films A-600 and B-600 films become transparent for wavelength $\lambda \gtrsim 580$ nm and $\gtrsim 670$ nm which corresponds to photon energies $E_{ph} \lesssim 1.8$ eV and 2.1 eV, respectively. A more thorough analysis employing a so-called Tauc plot making use of

$$(\alpha E_{ph})^2 = E_{ph} - E_g \tag{4}$$

where α is the absorption coefficient and E_{ph} is the photon energy [77], is shown in Fig. 14(b). A direct band gap as in the case of CuO and NiO is assumed [78,79]. The extracted optical band gaps are 2.01 eV and 2.11 eV for annealed films deposited at 2.8 Pa and 50 Pa, respectively.
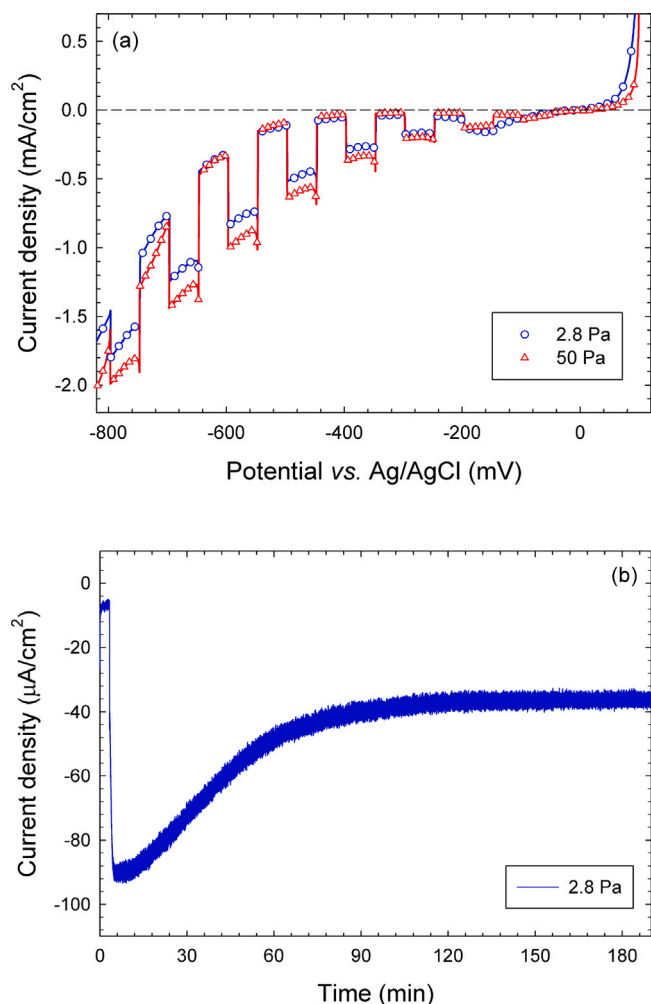
Fig. 16. GIXRD of annealed CuNiO films on FTO-coated soda lime glass at 50 Pa before and after 120 min of PEC activity measurements. Disappearing and newly appearing reflections are indicated by blue and red arrows, respectively. Reflections from NiO (▼), CuO (•), Cu$_2$O (▲), and from the FTO substrate (×) are indicated.

Fig. 15. (a) PEC activity (photocurrent density) *versus* applied potential of annealed films (600 °C) deposited on FTO-coated glass at 2.8 Pa (○) and 50 Pa (△). (b) Time dependence of photocurrent density at –300 mV vs. Ag/AgCl.

appear. The newly observed reflections are attributed to cubic Cu$_2$O. An oxygen reduction of CuO photocatalysts to Cu$_2$O was noted before [81]. The optical band gap of Cu$_2$O is larger compared to CuO which further explains the observed band gap increase (Fig. 15) [82]. The intensity of the NiO reflections are slightly reduced (about −15%). Significant changes of the NiO reflection pattern or the appearance of new reflections from nickel oxide are not observed, however.

5. Conclusions

Results for deposition of mixed copper nickel oxide films with the help of a pulsed hollow cathode (PHC) discharge operated at 5 kHz are reported. The PHC discharge is characterized by energy-resolved mass spectrometry and time-resolved optical emission spectroscopy. The ion mass spectrum is dominated by Ar$^+$, O$^+$ and O$_2^+$ ions from the working gas and sputtered Ni$^+$ and Cu$^+$ ions from the CuNi cathode. Optical emission spectroscopy shows the presence of strong Ar I and O I lines in the red part (746–782 nm) and of Cu I and Ni I lines in the ultraviolet part (318–354 nm) of the optical spectrum. The optical emission closely follows the time-dependence of the pulsed discharge. The investigated deposition rate increases with gas pressure in the vacuum chamber. It is explained by a more directed gas flow towards the substrate with the growing film. Deposited films are composed of a mixed metal oxide (MMO) cubic Cu$_x$Ni$_{1-x}$O phase with $x \approx 0.5$. Upon annealing at 600 °C, the MMO phase separates into CuO and NiO subphases. The PEC activity displays a photocathode behaviour. The PEC activity initially is rather large but drops to less than 40% of its initial value within the following 2 h. It is shown that this behaviour is related to the reduction of CuO to Cu$_2$O.

The optical band gap increases during PEC activity measurements, see below.

4.3. Photoelectrochemical (PEC) activity

Fig. 15(a) shows the PEC activity of the annealed Cu$_x$Ni$_{1-x}$O film deposited on FTO-coated glass. The investigated film acts as a photocathode and shows a large PEC activity similar to that of CuO [80] which forms a major phase of the annealed film, see Table 3. Unfortunately, the photoelectrochemical activity is not stable with time and drops to about 40 % of its initial value within 120 min, see Fig. 15(b). This photocorrosion effect is well-known for CuO [80,81]. In order to shed some light on the involved structural changes, the optical transmittance and the crystallographic structure of the films after PEC treatment was investigated. As shown in Fig. 14, the transmittance increases at wavelength below 600 nm while the extracted optical band gap increases from 2.11 eV to 2.45 eV and from 2.01 eV to 2.32 eV for films A-600 and B-600, respectively. GIXRD measurements of the A-600 sample before and after PEC activity measurements are displayed in Fig. 16. Significant differences between the two measurements are noted. The untreated A-600 sample shows reflections from monoclinic CuO (indicated by blue arrows) and NiO. The CuO reflections disappear during PEC treatment and new reflections (indicated by red arrows)
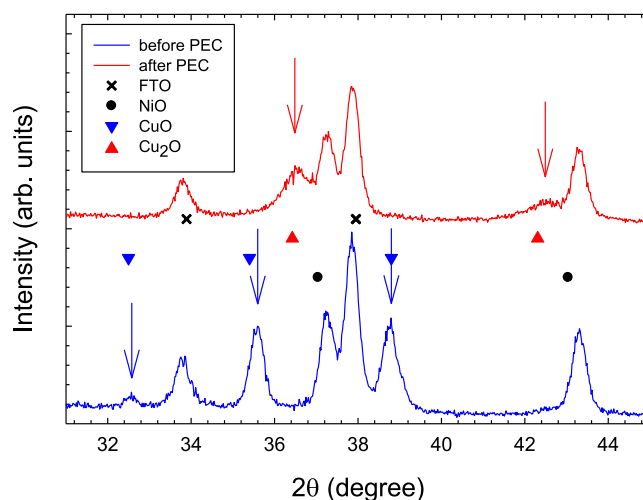
CRediT authorship contribution statement

Declaration of competing interest

The authors declare that they have no known competing financial interests or personal relationships that could have appeared to influence the work reported in this paper.

Data availability

Data will be made available on request.

Acknowledgements

References

[1] D. Klissurski, E. Uzunova, K. Ivanov, Binary spinel cobaltites of nickel, copper and zinc as precursors of catalysts for carbon oxides methanation, Catal. Lett. 15 (1992) 385.

[2] K. Angus, P. Thomas, J.-P. Guerbois, Synthesis and characterisation of cobaltite and ferrite spinels using thermogravimetric analysis and X-ray crystallography, J. Therm. Anal. Calorim. 108 (2012) 449, http://dx.doi.org/10.1007/s10973-011-1863-4.

[3] L. Tao, P. Guo, W. Zhu, T. Li, X. Zhou, Y. Fu, C. Yu, H. Ji, Highly efficient mixed-metal spinel cobaltite electrocatalysts for the oxygen evolution reaction, Chin. J. Catal. 41 (2020) 1855, http://dx.doi.org/10.1016/S1872-2067(20)63638-5.

[4] K. Li, R. Zhang, R. Gao, G.-Q. Shen, L. Pan, Y. Yao, K. Yu, X. Zhang, J.-J. Zou, Metal-defected spinel $Mn_xCo_3-xO_4$ with octahedral mn-enriched surface for highly efficient oxygen reduction reaction, Appl. Catal. B 244 (2019) 536, http://dx.doi.org/10.1016/j.apcatb.2018.11.072.

[5] K. Jiratova, P. Soukal, A. Kapran, T. Babii, J. Balabanova, M. Kostejn, M. Cada, J. Maixner, P. Topka, Z. Hubicka, F. Kovanda, Nickel-copper oxide catalysts deposited on stainless steel meshes by plasma jet sputtering: Comparison with granular analogues and synergistic effect in VOC oxidation, Catalysts 13 (2023) 595, http://dx.doi.org/10.3390/catal13030595.

[6] A. Faraz, A. Maqsood, N.M. Ahmad, Structural and electrical properties of magnetic ceramics of $Co_{1-x}Cu_xFe_2O_4$ spinel nanoferrites, Adv. Appl. Ceramics 111 (2012) 228, http://dx.doi.org/10.1179/1743676112Y.0000000001.

[7] L. Merabet, K. Rida, N. Boukmouche, Sol-gel synthesis, characterization, and supercapacitor applications of MCo_2O_4 (M = Ni, Mn, Cu, Zn) cobaltite spinels, Ceram. Int. 44 (2018) 11265, http://dx.doi.org/10.1016/j.ceramint.2018.03.171.

[8] S. Funahashi, E. Kobayashi, M. Kimura, Kosuke Shiratsuyu, C.A. Randall, Chelate complex assisted cold sintering for spinel ceramics, J. Ceram. Soc. Jpn. 127 (2019) 899, http://dx.doi.org/10.2109/jcersj2.19140.

[9] M.O. Senina, D.O. Lemeshev, V.A. Kolesnikov, Methods of synthesizing alumo-magnesium spinel powders for obtaining transparent ceramic (review), Glass Ceram. 74 (2018) 358, http://dx.doi.org/10.1007/s10717-018-9994-8.

[10] D. Darbar, M.R. Anilkumar, V. Rajagopalan, I. Bhattacharya, H.I. Elim, T. Ramakrishnappa, F.I. Ezema, R. Jose, M.V. Reddy, Ceram. Int. 44 (2018) 4630, http://dx.doi.org/10.1016/j.ceramint.2017.12.010.

[11] A. Sutka, K.A. Gross, Spinel ferrite oxide semiconductor gas sensors, Sensors Actuators B 222 (2016) 95, http://dx.doi.org/10.1016/j.snb.2015.08.027.

[12] J.M. Goncalves, L.V. de Faria, A.B. Nascimento, R.L. Germscheidt, S. Patra, L.P. Hernandez-Saravia, J.A. Bonacin, R.A.A. Munoz, L. Angnes, Sensing performances of spinel ferrites MFe_2O_4 (M = Mg, Ni, Co, Mn, Cu and Zn) based electrochemical sensors: a review, Anal. Chim. Acta 1233 (2022) 340362, http://dx.doi.org/10.1016/j.aca.2022.340362.

[13] H.-J. Kim, J.-H. Lee, Highly sensitive and selective gas sensors using p-type oxide semiconductors: Overview, Sensors Actuators B 192 (2014) 607, http://dx.doi.org/10.1016/j.snb.2013.11.005.

[14] A. Moumen, G.C.W. Kumarage, E. Comini, P-type metal oxide semiconductor thin films: Synthesis and chemical sensor applications, Sensors 22 (2022) 1359, http://dx.doi.org/10.3390/s22041359.

[15] E.M. Masoud, Improved initial discharge capacity of nanostructured Ni-Co spinel ferrite as anode material in lithium ion batteries, Solid State Ion. 253 (2013) 247, http://dx.doi.org/10.1016/j.ssi.2013.10.017.

[16] Q. He, S. Gu, T. Wu, S. Zhang, X. Ao, J. Yang, Z. Wen, Self-supported mesoporous $FeCo_2O_4$ nanosheets as high capacity anode material for sodium-ion battery, Chem. Engin. J. 330 (2017) 764, http://dx.doi.org/10.1016/j.cej.2017.08.014.

[17] Y. Sharma, N. Sharma, G.V. Subba Rao, B.V.R. Chowdari, Studies on spinel cobaltites, $FeCo_2O_4$ and $MgCo_2O_4$ as anodes for li-ion batteries, Solid State Ion. 179 (2008) 587, http://dx.doi.org/10.1016/j.ssi.2008.04.007.

[18] C.M. Julien, F. Gendron, A. Amdouni, M. Massot, Lattice vibrations of materials for lithium rechargeable batteries. VI: Ordered spinels, Mater. Sci. Eng. B 130 (2006) 41, http://dx.doi.org/10.1016/j.mseb.2006.02.003.

[19] W. Burgstaller, M. Hafner, M. Voith, A.I. Mardare, A.W. Hassel, Copper-nickel oxide thin film library reactively co-sputtered from a metallic sectioned cathode, J. Mater. Sci. 29 (2014) 148, http://dx.doi.org/10.1557/jmr.2013.336.

[20] M.T. Greiner, L. Chai, M.G. Helander, W.-M. Tang, Z.-H. Lu, Transition metal oxide work functions: The influence of cation oxidation state and oxygen vacancies, Adv. Funct. Mater. 22 (2012) 4557, http://dx.doi.org/10.1002/adfm.201200615.

[21] Y. Wang, H. Suzuki, J. Xie, O. Tomita, D.J. Martin, M. Higashi, D. Kong, R. Abe, J. Tang, Mimicking natural photosynthesis: Solar to renewable H_2 fuel synthesis by Z–scheme water splitting systems, Chem. Rev. 2018 (118) (2018) 5201, http://dx.doi.org/10.1021/acs.chemrev.7b00286.

[22] S. Nishioka, F.E. Osterloh, X. Wang, T.E. Mallouk, K. Maeda, Photocatalytic water splitting, Nat. Rev. Methods Primers 3 (2023) 42, http://dx.doi.org/10.1038/s43586-023-00226-x.

[23] T. Miyata, H. Tanaka, H. Sato, T. Minami, P-type semiconducting Cu_2O–NiO thin films prepared by magnetron sputtering, J. Mater. Sci. 41 (2006) 5531, http://dx.doi.org/10.1007/s10853-006-0271-9.

[24] O. Selmi, H. Bouzid, H. Saidi, A. Bouazizi, The effect of copper doping on the optical and electrical properties of nickel oxide thin films deposited by spin coating technique, Emergent Mater. 5 (2022) 1033, http://dx.doi.org/10.1007/s42247-021-00305-3.

[25] T.C. Tasdemirci, Synthesis of copper-doped nickel oxide thin films: Structural and optical studies, Chem. Phys. Lett. 738 (2020) 136884, http://dx.doi.org/10.1016/j.cplett.2019.136884.

[26] H. El Aakib, J.F. Pierson, M. Chaik, H. Ait Dads, C. Samba Vall, A. Narjis, A. Outzourhit, Nickel doped copper oxide thin films prepared by radiofrequency reactive sputtering: study of the impact of nickel content on the structural, Opt. Electr. Propert. Spectros. Lett. 54 (2019) 487, http://dx.doi.org/10.1080/00387010.2018.1560335.

[27] S. Mani Menaka, G. Umadevi, M. Manickam, Effect of copper concentration on the physical properties of copper doped NiO thin films deposited by spray pyrolysis, Mater. Chem. Phys. 191 (2017) 181.

[28] F. Cao, S. Guo, H. Ma, G. Yang, S. Yang, J. Gong, Highly sensitive nonenzymatic glucose sensor based on electrospun copper oxide-doped nickel oxide composite microfibers, Talanta 86 (2011) 214, http://dx.doi.org/10.1016/j.talanta.2011.09.003.

[29] S. Wojtyla, T. Baran, Copper-nickel-oxide nanomaterial for photoelectrochemical hydrogen evolution and photocatalytic degradation of volatile organic compounds, Mater. Res. Bull. 142 (2021) 111418, http://dx.doi.org/10.1016/j.materresbull.2021.111418.

[30] Amna Bashir, Jia Haur Lew, Sudhanshu Shukla, Disha Gupta, Tom Baikie, Sudip Chakraborty, Rahul Patidar, Annalisa Bruno, Subodh Mhaisalkar, Zareen Akhter, Cu-doped nickel oxide interface layer with nanoscale thickness for efficient and highly stable printable carbon-based perovskite solar cell, Sol. Energy 182 (2019) 225, http://dx.doi.org/10.1016/j.solener.2019.02.056.

[31] M.S. Vasil'eva, V.S. Rudnev, O.E. Sklyarenko, L.M. Tyrina, N.B. Kondrikov, Titanium-supported nickel–copper oxide catalysts for oxidation of carbon(II) oxide, Russ. J. Gen. Chem. 80 (2010) 1557, http://dx.doi.org/10.1134/S1070363210080037.

[32] Anita Sagadevan Ethiraj, Prateek Uttam, Varunkumar K, Kwok Feng Chong, Gomaa A.M. Ali, Photocatalytic performance of a novel semiconductor nanocatalyst: Copper doped nickel oxide for phenol degradation, Mater. Chem. Phys. 242 (2020) 122520, http://dx.doi.org/10.1016/j.matchemphys.2019.122520.

[33] J. Blanco, P. Avila, S. Suarez, M. Yates, J.A. Martin, L. Marzo, C. Knapp, CuO/NiO monolithic catalysts for NO_x removal from nitric acid plant flue gas, Chem. Eng. J. 97 (2004) 1, http://dx.doi.org/10.1016/S1385-8947(03)00085-8.

[34] C. Ravi Dhas, S. Esther Santhoshi Monica, K. Jothivenkatachalam, A. Joseph Nathanael, V. Kavinkumar, R. Venkatesh, D. Arivukarasan, Direct-grown nebulizer-sprayed nickel-copper mixed metal oxide nanocomposite films as bifunctional electrocatalyst for water splitting, Ionics 28 (2022) 383, http://dx.doi.org/10.1007/s11581-021-04285-6.

[35] V.I. Kolobov, L.D. Tsendin, Plasma sources, Sci. Technol. 4 (1995) 551.

[36] J.P. Boeuf, L.C. Pitchford, Field reversal in the negative glow of a DC glow discharge, J. Phys. D: Appl. Phys. 28 (1995) 2083, http://dx.doi.org/10.1088/0022-3727/28/10/013.

[37] G.J.M. Hagelaar, D.B. Mihailova, J. van Dijk, Analytical model of a longitudinal hollow cathode discharge, J. Phys. D: Appl. Phys. 43 (2010) 465204, http://dx.doi.org/10.1088/0022-3727/43/46/465204.

[38] M. Tichy, Z. Hubicka, M. Sicha, M. Cada, J. Olejnicek, O. Churpita, L. Jastrabik, P. Virostko, P. Adamek, P. Kudrna, S. Leshkov, M. Chichina, S. Kment, Langmuir probe diagnostics of a plasma jet system, Plasma Sources. Sci. Technol. 18 (2009) 014009, http://dx.doi.org/10.1088/0963-0252/18/1/014009.

[39] D. Ishikawa, S. Hasegawa, Development of removable hollow cathode discharge apparatus for sputtering solid metals, J. Spectroscopy 2019 (2019) 7491671, http://dx.doi.org/10.1155/2019/7491671.

[40] K. Ishii, High rate low kinetic energy gas flow sputtering system, J. Vacuum Sci. Technol. A 7 (1989) 256, http://dx.doi.org/10.1116/1.576129.

[41] H. Koch, L.J. Friedrich, V. Hinkel, F. Ludwig, B. Politt, T. Schurig, Hollow cathode discharge sputtering device for uniform large area thin film deposition, J. Vac. Sci. Technol. A 9 (1991) 2374, http://dx.doi.org/10.1116/1.577279.

[42] Z. Hubicka, Hollow cathodes and plasma jets for thin film deposition, in: R. Hippler, H. Kersten, M. Schmidt, K.H. Schoenbach (Eds.), Low Temperature Plasmas, Vol. 2, Wiley-VCH Verlag, Weinheim, 2008, p. 715.

[43] A. Lunk, Plasma activated physical vapour deposition by hollow cathode arc, Vacuum 41 (1990) 1965.

[44] Z. Hubicka, M. Cada, P. Adamek, P. Virostko, J. Olejnicek, A. Deyneka, L. Jastrabik, K. Jurek, G. Suchaneck, M. Guenther, G. Gerlach, P. Bohac, Investigation of the RF pulse modulated plasma jet system during the deposition of PbZr$_x$Ti$_{1-x}$O$_3$ thin films on polymer substrates, Surf. Coat. Technol. 200 (2005) 940, http://dx.doi.org/10.1016/j.surfcoat.2005.02.041.

[45] F. Paschen, Bohrs heliumlinien, Ann. Phys. IV 50 (1916) 901, http://dx.doi.org/10.1002/andp.19163551603.

[46] D.W. Duquette, J.E. Lawler, Radiative lifetimes in Nb I, Phys. Rev. A 26 (1982) 330, http://dx.doi.org/10.1103/PhysRevA.26.330.

[47] J. Olejnicek, J. Smid, M. Cada, P. Ksirova, M. Kohout, R. Perekrestov, D. Tvarog, S. Kment, H. Kmentova, Z. Hubicka, High rate deposition of photoactive TiO$_2$ films by hot hollow cathode, Surf. Coat. Technol. 383 (2020) 125256, http://dx.doi.org/10.1016/j.surfcoat.2019.125256.

[48] J. Olejnicek, J. Smid, R. Perekrestov, P. Ksirova, J. Rathousky, M. Kohout, M. Dvorakova, S. Kment, K. Jurek, M. Cada, Z. Hubicka, Co$_3$O$_4$ thin films prepared by hollow cathode discharge, Surf. Coat. Technol. 366 (2019) 303, http://dx.doi.org/10.1016/j.surfcoat.2019.03.010.

[49] J. Olejnicek, A. Hrubantova, L. Volfova, M. Dvorakova, M. Kohout, D. Tvarog, O. Gedeon, H. Wulff, R. Hippler, Z. Hubicka, WO$_3$ and WO$_3 - x$ thin films prepared by DC hollow cathode discharge, Vacuum 195 (2022) 110679, http://dx.doi.org/10.1016/j.vacuum.2021.110679.

[50] R. Hippler, M. Cada, Z. Hubicka, A positively biased external anode for energy control of plasma ions: hollow cathode and magnetron sputtering discharge, Plasma Sources. Sci. Technol. 30 (2021) 045003, http://dx.doi.org/10.1088/1361-6595/abe0cc.

[51] W. Jitschin, Strömung von Gasen, in: K. Joosten (Hrsg.) (Ed.), Wutz Handbuch Vakuumtechnik, Vieweg+Teubner Verlag, Springer Fachmedien, 2004, http://dx.doi.org/10.1007/978-3-322-96971-2.

[52] M. Sicha, L. Bardos, M. Tichy, L. Soukup, L. Jastrabik, H. Barankova, R.J. Soukup, J. Tous, Simple physical model of generation of the low-pressure radio frequency supersonic plasma jet, Contrib. Plasma Phys. 34 (1994) 749.

[53] E.W. Lemmon, R.T. Jacobsen, Viscosity and thermal conductivity equations for nitrogen, oxygen, argon, and air, Int. J. Thermophy 25 (2004) 21, http://dx.doi.org/10.1023/B:IJOT.0000022327.04529.f3r.

[54] Z. Hubicka, G. Pribil, R.J. Soukup, N.J. Ianno, Investigation of the rf and dc hollow cathode plasma-jet sputtering systems for the deposition of silicon thin films, Surf. Coat. Technol. 160 (2002) 114.

[55] R. Hippler, M. Cada, V. Stranak, Z. Hubicka, C.A. Helm, Pressure dependence of Ar$_2^+$, ArTi$^+$, and Ti$_2^+$ dimer formation in a magnetron sputtering discharge, J. Phys. D: Appl. Phys. 50 (2017) 445205.

[56] R. Hippler, M. Cada, V. Stranak, C.A. Helm, Z. Hubicka, Pressure dependence of singly and doubly charged ion formation in a HiPIMS discharge, J. Appl. Phys. 125 (2019) 013301, http://dx.doi.org/10.1063/1.5055356.

[57] K.J.R. Rosman, P.D.P. Taylor, Isotopic compositions of the elements 1997(Technical Report), Pure Appl. Chem 70 (1998) 217, http://dx.doi.org/10.1351/pac199870010217.

[58] T. Welzel, M. Kellermeier, K. Harbauer, K. Ellmer, Development of a compact combined plasma sensor for plasma surface engineering processes, Appl. Phys. Lett. 102 (2013) 211605, http://dx.doi.org/10.1063/1.4807892.

[59] R. Hippler, M. Cada, Z. Hubicka, Ion energy distribution of plasma ions of a hollow cathode discharge in Ar + N$_2$ and Ar + O$_2$ gas mixtures, Eur. Phys. J. D 2022 (76) (2022) 214, http://dx.doi.org/10.1140/epjd/s10053-022-00539-8.

[60] N.G. Schmahl, J. Barthel, G.F. Eikerling, Röntgenographische untersuchungen an den systemen MgO-CuO und NiO-CuO, Z. Anorg. Allg. Chem. 332 (1964) 230, http://dx.doi.org/10.1002/zaac.19643320503.

[61] E.J. Angelin, R. Hippler, Negatively and positively charged oxygen ion formation in collisions of positively charged projectiles with O2 molecules in the energy range 50-350 keV, J. Phys. B: At. Mol. Opt. Phys. 47 (2014) 225208, http://dx.doi.org/10.1088/0953-4075/47/22/225208.

[62] Atomic spectra database, in: NIST Standard Reference Database Vol. 78, http://dx.doi.org/10.18434/T4W30F, (Retrieved 11 August 2022).

[63] M. Tichy, Z. Hubicka, M. Sicha, M. Cada, J. Olejnicek, O. Churpita, L. Jastrabik, P. Virostko, P. Adamek, P. Kudrna, S. Leshkov, M. Chichina, S. Kment, Langmuir probe diagnostics of a plasma jet system, Plasma Sources. Sci. Technol. 18 (2009) 014009, http://dx.doi.org/10.1088/0963-0252/18/1/014009.

[64] M. Tichy, M. Sicha, L. Bardos, L. Soukup, L. Jastrabik, K. Kapoun, J. Tous, Z. Mazanec, R.J. Soukup, A study of the gas flow in the RF low-pressure supersonic jet plasma chemical system, Contrib. Plasma Phys. 34 (1994) 765.

[65] S. Sasaki, K. Fujino, Y. Takeuchi, X-ray determination of electron-density distributions in oxides, MgO, MnO, CoO, and NiO, and atomic scattering factors of their constituent atoms, Proc. Japan Academy Ser. B 55 (1979) 43, http://dx.doi.org/10.2183/pjab.55.43.

[66] S. Chatterjee, A. Ray, M. Mandal, S. Das, S.K. Bhattacharya, Synthesis and characterization of cuo-nio nanocomposites for electrochemical supercapacitors, J. Mat. Eng. Perf. (JMEPEG) 29 (2020) 8036, http://dx.doi.org/10.1007/s11665-020-05261-3.

[67] A.Y. Faid, A.O. Barnett, F. Seland, S. Sunde, NiCu mixed metal oxide catalyst for alkaline hydrogen evolution in anion exchange membrane water electrolysis, Electrochim. Acta 371 (2021) 137837, http://dx.doi.org/10.1016/j.electacta.2021.137837.

[68] S.C. Chen, T.Y. Kuo, S.U. Jend, H.P. Chiang, W.Y. Liu, C.H. Wang, Effect of copper content on the electrical stability of nickel oxide films, Thin Solid Films 584 (2015) 238, http://dx.doi.org/10.1016/j.tsf.2014.11.085.

[69] S. Åsbrink, L.-J. Norrby, A refinement of the crystal structure of copper(II) oxide with a discussion of some exceptional e.s.d.'s, Acta Crystallograph. B 26 (1970) 8, http://dx.doi.org/10.1107/S0567740870001838.

[70] R. Restori, D. Schwarzenbach, Charge density in cuprite, Cu$_2$O, Acta Crystallograph. B 42 (1986) 201, http://dx.doi.org/10.1107/S0108768186098336.

[71] A. Javadian, M.R. Fadavieslam, Impact of copper doping in NiO thin films deposited by spray pyrolysis on their physical properties, J. Mater. Sci. Mater. Electron. 33 (2022) 23362, http://dx.doi.org/10.1007/s10854-022-09098-5.

[72] C. Mahala, M. Basu, Nanosheets of NiCo$_2$O$_4$/NiO as efficient and stable electrocatalyst for oxygen evolution reaction, ACS Omega 2017 (2) (2017) 7559, http://dx.doi.org/10.1021/acsomega.7b00957.

[73] W.J. Duan, S.H. Lu, Z.L. Wu, Y.S. Wang, Size effects on properties of NiO nanoparticles grown in alkalisalts, J. Phys. Chem. C 116 (2012) 26043, http://dx.doi.org/10.1021/jp308073c.

[74] N. Mironova-Ulmane, A. Kuzmin, I. Sildos, L. Puust, J. Grabis, Magnon and phonon excitations in nanosized NiO, Latvian J. Phys. Tech. Sci. 56 (2019) 61, http://dx.doi.org/10.2478/lpts-2019-0014.

[75] P.S. Murthy, V.P. Venugopalan, D.D. Arunya, S. Dhara, R. Pandiyan, A.K. Tyagi, Antibiofilm activity of nano sized CuO, in: International Conference on Nanoscience, Engineering and Technology, ICONSET 2011, 2011, p. 580, http://dx.doi.org/10.1109/ICONSET.2011.6168037.

[76] A.V. Fedorov, R.G. Kukushkin, P.M. Yeletsky, O.A. Bulavchenko, Y.A. Chesalov, V.A. Yakovlev, Temperature-programmed reduction of model CuO, NiO and mixed CuO-NiO catalysts with hydrogen, J. Alloys Compd. 844 (2020) 15613, http://dx.doi.org/10.1016/j.jallcom.2020.156135.

[77] J. Tauc, R. Grigorovic, A. Vancu, Optical properties and electronic structure of amorphous germanium, Phys. Status Solidi 15 (1966) 627.

[78] W.-J. Lee, X.-J. Wang, Structural, optical, and electrical properties of copper oxide films grown by the SILAR method with post-annealing, Coatings 11 (2021) 864, http://dx.doi.org/10.3390/coatings11070864.

[79] K.N. Manjunatha, S. Paul, Investigation of optical properties of nickel oxide thin films deposited on different substrates, Appl. Surf. Sci. 352 (2015) 10, http://dx.doi.org/10.1016/j.apsusc.2015.03.092.

[80] M. Neumann-Spallart, P. Singh, S. Pausova, A. Mishra, D. Bhagat, H. Krysova, I. Mukhopadhyay, J. Krysa, p-CuO films and photoelectrochemical corrosion, J. Electroanal. Chem. 919 (2022) 116555, http://dx.doi.org/10.1016/j.jelechem.2022.116555.

[81] Z. Hubicka, M. Zlamal, M. Cada, S. Kment, J. Krysa, Photo-electrochemical stability of copper oxide photocathodes deposited by reactive high power impulse magnetron sputtering, Catal. Today 328 (2019) 29, http://dx.doi.org/10.1016/j.cattod.2018.11.034.

[82] Y. Wang, S. Lany, J. Ghanbaja, Y. Fagot-Revurat, Y.P. Chen, F. Soldera, D. Horwat, F. M´ucklich, J.F. Pierson, Electronic structures of Cu2O, Cu4O3, and CuO: A joint experimental and theoretical study, Phys. Rev. B 94 (2016) 245418, http://dx.doi.org/10.1103/PhysRevB.94.245418.